Intense low-noise terahertz generation by relativistic laser irradiating near-critical-density plasma

Shijie Zhang(张世杰)[1,2], Weimin Zhou(周维民)[2,†], Yan Yin(银燕)[1], Debin Zou(邹德滨)[1], Na Zhao(赵娜)[4], Duan Xie(谢端)[5], and Hongbin Zhuo(卓红斌)[3,‡]

[1] *Department of Physics, National University of Defense Technology, Changsha* 410073, *China*
[2] *Science and Technology on Plasma Physics Laboratory, Laser Fusion Research Center, China Academy of Engineering Physics (CAEP), Mianyang* 621900, *China*
[3] *Center for Advanced Material Diagnostic Technology, Shenzhen Technology University, Shenzhen* 518118, *China*
[4] *School of Microelectronics and Physics, Hunan University of Technology and Business, Changsha* 410205, *China*
[5] *School of Electronic Information and Electrical Engineering, Changsha University, Changsha* 410003, *China*

(Received 13 May 2022; revised manuscript received 7 July 2022; accepted manuscript online 5 August 2022)

Low-noise terahertz (THz) radiation over 100 MV/cm generation by a linearly-polarized relativistic laser pulse interacting with a near-critical-density (NCD) plasma slab is studied by theory and particle-in-cell (PIC) simulations. A theoretical model is established to examine the dipole-like radiation emission. The THz radiation is attributed to the single-cycle low-frequency surface current, which is longitudinally constrained by the quasi-equilibrium established by the laser ponderomotive force and the ponderomotively induced electrostatic force. Through theoretical analysis, the spatiotemporal characteristics, polarization property of the THz radiation, and the relation between the radiation strength with the initial parameters of driving laser and plasma are obtained, which are in good consistence with the PIC simulation results. Furthermore, it is found by PIC simulations that the generation of thermal electrons can be suppressed within the appropriate parameter regime, resulting in a clear THz radiation waveform. The appropriate parameter region is given for generating a low-noise intense THz radiation with peak strength reaching 100 MV/cm, which could find potential applications in nonlinear THz physics.

Keywords: intense terahertz radiation, relativistic laser–plasma interactions, particle-in-cell simulation

PACS: 52.65.Rr, 52.59.–f, 52.38.–r, 52.38.Kd **DOI:** 10.1088/1674-1056/ac872c

1. Introduction

THz radiation has attracted significant attention during the last few decades for its exclusive properties.[1,2] THz pulses with a field over 1 MV/cm are important for nonlinear lattice excitations,[3] insulator-to-metal transitions,[4] photo-induced superconductivity,[5] and ultrafast control of ferroelectric polarization.[6] More intense milli-Joule (mJ) THz wave with field strength over GV/m can be applied to nonlinear pump-probe experiments[7–9] or provide opportunities for high-gradient acceleration of electrons.[10–14] Conventionally, gigantic accelerator facilities[15,16] and nonlinear crystals[17–19] are mainly used to produce intense THz radiation. Compared with these traditional methods, laser-produced plasmas have recently acted as promising drivers toward high-power, low-cost and table-top THz emissions.[20] In particular, solid-density plasma targets are expected to produce stronger radiations than gas targets, because they can withstand quite a high laser pump intensity, and more electrons can participate in the radiation generation process.

When the laser pulse interacts with the solid slab, a large number of hot electrons are generated on the front. Among them, electrons with sufficient high longitudinal velocity can escape from the laser field, and then go deep into the target. When these electrons pass through the vacuum interface of the rear target, due to the discontinuity of the dielectric, they will produce a transverse transient current and emit coherent transition radiation (CTR).[21–24] An electron sheath is formed behind the target to produce a strong electrostatic field. The low-energy part of the electrons is reflected by the sheath field and undergoes deceleration and acceleration in the sheath field, thus emitting bremsstrahlung-like radiation (BR).[25] In addition, the number and velocity of electrons in the sheath vary with time, resulting in a time-varying current. Then, the changing current generates electromagnetic radiation referred to as sheath radiation (SR).[26–30] The parameter range of these three THz generation mechanisms was discussed in detail in Ref. [31]. Generally, in the process of THz generation, a variety of mechanisms related to hot electrons coexist, which distorts the THz waveform to a certain extent.

In this paper, we propose a scheme to produce intense low-noise THz by reducing the density of the plasma slab from solid density to near-critical density ranging from $1.0n_c$ to $4.0n_c$, where n_c is the critical density. Such a near-critical-density (NCD) plasma slab can be fabricated by high-pressure

†Corresponding author. E-mail: hongbin.zhuo@gmail.com
‡Corresponding author. E-mail: zhouwm@caep.cn

© 2023 Chinese Physical Society and IOP Publishing Ltd

gas[32,33] in the laboratory. When the sharp-edged plasma slab is irradiated by a linearly polarized laser pulse which is not transparent to the slab, the surface electrons on the front side of the target are first compressed into a thin layer by the laser ponderomotive force, and at the same time, the electron layer is dragged back by the ponderomotively induced charge-separation electrostatic force. Within the parameter range of our scheme, the ponderomotive force and electrostatic force are in quasi-equilibrium. This quasi-equilibrium makes the surface electrons move collectively and stably in the quite thin layer of the target. During this process, the escape of hot electrons, which usually occurs at solid density, is suppressed in the NCD target. Thus, the radiation noises related with thermal electrons no longer emerge. The single-cycle longitudinal motions of these surface electrons induce a surface current which gives off the dipole-like THz emission at the front surface. Although the longitudinal velocity of these source electrons is not very high, because few surface electrons can escape, and the radiation of source electrons is highly coherent, intense THz pulses over 100 MV/cm can still be produced. A simple model is established to study the angular, spatial distribution, and polarization properties of the radiation. The effectiveness of the scheme is verified by particle-in-cell (PIC) simulation. The radiation characteristics and the dependence of radiation intensity on the initial parameters of the incident laser and plasma target are all in good consistence with the theoretical predictions.

2. Theoretical analysis

As shown in Fig. 1(a), a spherical coordinate with zenith direction pointing to $+x$ direction is established. Here r, θ, and φ are the radical distance, polar angle, and azimuthal angle; $\hat{r}$, $\hat{\theta}$, and $\hat{\varphi}$ are the corresponding unit vectors, respectively. A sharp-edged plasma slab with near-critical density is normally irradiated by a linearly polarized relativistic laser pulse incident from the left boundary. The slight imbalance between the ponderomotive force and the charge-separation field can excite a low-frequency longitudinal current on the front surface where the electrons are compressed into a very thin layer. The duration of the current is roughly the same as that of the driving laser, so the radiation frequency is almost near the carrier frequency of the driving pulse's envelope. The carrier frequency of the laser pulse with a duration of 100 fs is 10 THz. Considering a circular current source with radius w, the far-zone interference enhancement of radiation with wavelength λ_{T} at observation angle θ is described by the interference factor:[34]

$$F(\theta)=\left[J_1\left(\frac{2\pi w_0}{\lambda_{\mathrm{T}}}\sin\theta\right)\Big/\sin\theta\right]^2. \tag{1}$$

Here, J_1 is the Bessel function of the first order. If the transverse size of the current source is much less than the radiation wavelength, i.e., $w_0 \ll \lambda_{\mathrm{T}}$, $F(\theta)$ is almost constant. Thus, the circular source can be taken as a point source whose radiation is highly coherent. The radiation is like a spherical wave that propagates perpendicularly to a spherical wave-front centered at the laser spot, as shown in Fig. 1(c).

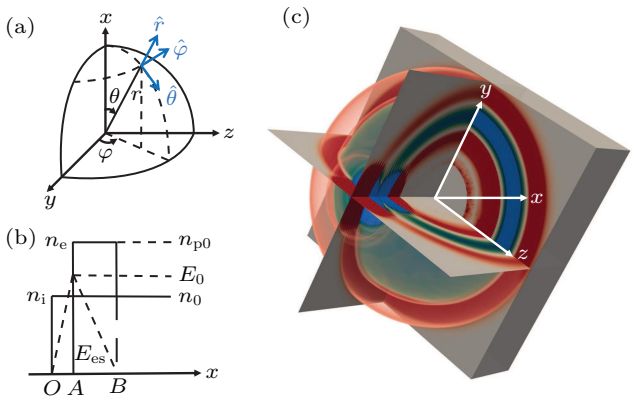


Fig. 1. (a) The schematic of the spherical coordinate system. (b) The schematic of the model for the motion of the surface electron layer. (c) The three-dimensional spatial distribution of THz radiation.

A simple model is used to illustrate the low-frequency motion of the surface electron layer,[35] as shown in Fig. 1(b). When the rising edge of the laser pulse arrives at the plasma surface, the surface electrons can be pushed forward by the ponderomotive force. Electrons then pile up with uniform density n_{p0} in the compression layer (between AB), leaving behind a charge depletion layer (between OA) where ions are inertially confined, and giving rise to a strong electrostatic field E_{es}. According to the Poisson equation, E_{es} is supposed to be of linear profile in the depletion layer with $E_{\mathrm{es}}=E_0 x/d$ and in the compression layer with $E_{\mathrm{es}}=[1-(x-d)/l_{\mathrm{s}}]E_0$. Here, $E_0=en_0 d/\varepsilon_0$ is the maximal electrostatic field, d denotes the displacement for the front surface of the compression layer; $l_{\mathrm{s}}=c/\omega_{\mathrm{pe}}=c\sqrt{\varepsilon_0 m_{\mathrm{e}}/n_{\mathrm{p0}}e^2}$ is the skin depth of laser pulse in compression layer, in which c is the light speed, ω_{pe} the frequency of electron plasma wave in compression layer, ε_0 the permittivity of vacuum, n_0 the initial electron number density, m_{e} and e the electron mass and charge, respectively.

The movement of the surface electron layer is determined by the pressure imbalance between ponderomotive and space-charge force:

$$\frac{\mathrm{d}(n_{\mathrm{p0}}l_{\mathrm{s}}p_x)}{\mathrm{d}t}=F_{\mathrm{px}}-\frac{eE_0n_{\mathrm{p0}}l_{\mathrm{s}}}{2}, \tag{2}$$

where the laser pressure is $F_{\mathrm{px}}=2I(1-\beta_x)/c(1+\beta_x)$. The intensity of linearly polarized pulse is $I=2\pi^2\varepsilon_0 a^2 m_{\mathrm{e}}^2 c^5/e^2\lambda_0^2$. Together with charge conservation $n_{\mathrm{p0}}l_{\mathrm{s}}=n_0(x+l_{\mathrm{s}})$, the relativistic motion of the electron layer can be written in normalized quantities as[36]

$$\frac{\mathrm{d}(\gamma_x\beta_x)}{\mathrm{d}\tau}=\frac{4a^2}{N_0}\frac{1}{X+\sqrt{X^2+1/\pi^2N_0}}\frac{1-\beta_x}{1+\beta_x}-4\pi^2N_0X. \tag{3}$$

Here, $a = eE/m_e\omega_0 c$ is the normalized laser amplitude, in which $\omega = 2\pi c/\lambda_0$ is laser frequency, and λ_0 is laser wavelength; $\gamma_x = 1/\sqrt{1-\beta_x^2}$ is relativistic factor. $X = x/\lambda_0$, $\beta_x = \mathrm{d}x/c\,\mathrm{d}t$, $\tau = t/T_0$ are the quantities normalized by wave length, light speed, laser period, respectively. $N_0 = n_0/n_c$ is normalized by the critical density $n_c = \omega_0^2\varepsilon_0 m_e/e^2$. Together with initial conditions $X(0) = 0$ and $\beta_x(0) = 0$, the exact solution of displacement and speed can be numerically calculated from Eq. (3).

In the near-critical-density regime, take $a_0 = 1.0$ and $N_0 = 2.0$ as an example, the maximal velocity calculated from Eq. (3) is $\beta_x \sim 0.01$, which is much less than light speed. This means that a quasi-static balance between laser pressure and charge-separation force is established. Thus, the longitudinal motion of the surface electron layer can be simplified to a quasi-static form

$$\frac{4a^2}{N_0}\frac{1}{X+\sqrt{X^2+1/\pi^2 N_0}} = 4\pi^2 N_0 X. \tag{4}$$

Then the displacement of the electron layer surface under the quasi-static condition is

$$X = \frac{a^2}{N_0\pi\sqrt{2a^2+N_0}}. \tag{5}$$

Taking X into the normalized equation $L_s = (2\pi)^{-1}\left(N_{p0}\right)^{-1/2}$ and $N_{p0}L_s = N_0(X+L_s)$, we can obtain $N_{p0} = 2a^2+N_0$ and $L_s = (2\pi)^{-1}\left(2a^2+N_0\right)^{-1/2}$. Here, L_s is the skin depth of the compression layer normalized by λ_0, and N_{p0} is the number density of the compression layer normalized by n_c. After calculating β_x and N_{p0}, we can determine the current source $j_x = -eN_{p0}n_c c\beta_x$. The current emits THz radiation that propagates into the vacuum. The retarded vector potential of the radiation is determined by[37]

$$A_x(r,t) = \frac{1}{4\pi\varepsilon_0 c^2}\int\frac{j_x(r',t-r/c)}{r}\,\mathrm{d}V'. \tag{6}$$

The superscript is used for the physical quantities at the source zone. This formula indicates that the vector potential at (r,t) is determined by the current source at the retarded time $t-r/c$. At the far-zone observation point, r can be regarded as a constant. Considering the transverse Gaussian distribution of laser intensity, the volume integration of j_x equals $-\int en_{p0}c\beta_x l_s 2\pi r'\,\mathrm{d}r'$. In terms of normalized quantities, the vector potential could be expressed as

$$\frac{eA_x(R,\tau)}{m_e c} = -\frac{1}{2R}\int\frac{\beta_x(R',\tau-R)}{L_s(R',\tau-R)}R'\,\mathrm{d}R'. \tag{7}$$

On the left side of Eq. (7), the vector potential is normalized by $m_e c/e$. R and R' are radial coordinates normalized by λ_0. $A_x(R,\tau)$ can be numerically acquired by integration according to Eq. (7).

Taking $\boldsymbol{A} = A_x(R,\tau)\hat{e}_{\boldsymbol{x}}$ into $\boldsymbol{B} = \nabla\times\boldsymbol{A}$ and using the formula for curl in the spherical coordinate system, we have $B_r = 0$, $B_\theta = 0$, and $B_\varphi(R,\theta,\tau) = -\partial A_x(R,\tau)\sin\theta/(\lambda_0\partial R)$. For spherical radiation, $A_x(R,\tau)$ has dependence on $\tau-R$. Replace $-\partial/\partial R$ by $\partial/\partial\tau$, the magnetic field can be expressed in normalized form as

$$\frac{eB_\varphi(R,\theta,\tau)}{m_e\omega_0} = \frac{1}{2\pi}\frac{\partial}{\partial\tau}\left[\frac{eA_x(R,\tau)}{m_e c}\right]\sin\theta. \tag{8}$$

Because $\boldsymbol{E}\times\boldsymbol{B} = \boldsymbol{S}$ and energy flux vector $\boldsymbol{S}$ points to the positive r direction, the electric field has only the θ component with $E_\theta = cB_\varphi$.

The vector potential in Eq. (6) is used for the three-dimensional (3D) situation. For the two-dimensional (2D) simulation (at the xy plane) which is symmetric along the z direction, vector potential has the following form:

$$A_x(r,t) = \frac{1}{2\pi c}\frac{1}{\varepsilon_0}\int_0^t\mathrm{d}t'\iint_{r\le c(t-t')}\frac{j_x(r',t')}{\left[c^2(t-t')^2-r^2\right]^{1/2}}\,\mathrm{d}S'. \tag{9}$$

For the 3D situation, $A_x(r,t)$ in Eq. (6) is solely determined by $j_x(r',t')$ at retarded time $t' = t-r/c$. However, for the 2D situation, $A_x(r,t)$ is determined by $j_x(r',t')$ at times earlier than the retarded time, i.e., $t' \le t-r/c$. This wake effect results from the lateral points on the line perpendicular to the 2D simulation plane, and will quickly disappear to zero. $A_x(r,t)$ in the 2D situation can be simplified to a normalized form as

$$\frac{eA_x(R,\tau)}{m_e\omega_0} = -\frac{1}{\pi}\int_0^{\tau-R}\frac{\mathrm{d}\tau'}{\left[(\tau-\tau')^2-R^2\right]^{1/2}} \times\int\frac{\beta_x(R',\tau')}{L_s(R',\tau')}\,\mathrm{d}R'. \tag{10}$$

To keep the direction of the field in the 2D simulation as the same as those in the xy plane (at $z=0$) in the 3D spherical coordinate, we define in the 2D situation that $B_\varphi = B_z$ for $y>0$ and $B_\varphi = -B_z$ for $y<0$.

3. PIC simulations

Two-dimensional PIC simulations are performed to check the validity of our analytical model by using the relativistic PIC code EPOCH.[38] A linearly polarized Gaussian laser pulse, whose electric field oscillates in the z direction, is normally incident from the left boundary and focused on the front surface of the plasma slab positioned at $x = 0$. The normalized intensity of laser pulse at the focus plane is $a_0 = a\sin^2(\pi\tau/\tau_L)\exp(-R'^2/W_0^2)$. Here, the normalized laser intensity maximum is $a_0 = 1.0$. The pulse duration is $\tau_L = 30.0$ and the waist radius is $W_0 = 5.0$. The wavelength is $\lambda_0 = 1$ μm. The laser parameters correspond to $I_0\lambda_0^2 \sim 1.37\times10^{18}$ W·cm^{-2}·μm^2, which is the relativistic threshold. The fully ionized plasma slab is 2 μm thick and consists of protons and electrons with an initial density of $n_0 = 2.0n_c$. The initial temperature of the electrons is zero. The size of the simulation box is $100\lambda_0\times100\lambda_0$ and the spatial resolution is up to 30 cells per wavelength, with each cell containing 50 protons and 50 electrons. For reference, the initial time $\tau = 0$ is set at the moment when the rising edge of the pulse impinges on the left surface of the target.

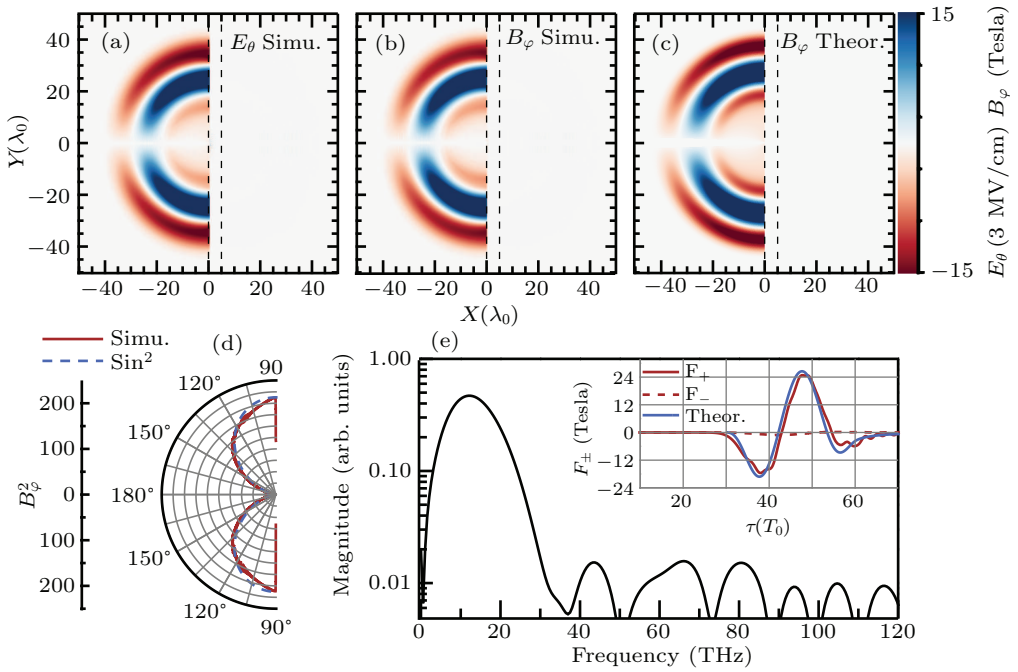


Fig. 2. The snapshot of radiation field (a) E_θ and (b) B_φ averaged in one laser cycle from simulation. (c) The snapshot of B_φ indicated by formula (8). The electric field is in units of 3.0 MV/cm, and the magnetic field is in units of Tesla. (d) The angular distribution of B^2_φ, where the red solid line represents the simulation result and the blue dashed line represents the sin-square fitting. (e) The inset plot gives the temporal spectrum of $F_\pm$ by simulation (red line) and theory (blue line). The main plot gives the corresponding frequency spectra of F_+.

Figures 2(a) and 2(b) show the snapshot of electric field $E_\theta = \pm E_y \cos\theta - E_x \sin\theta$ in units of 3.0 MV/cm and the magnetic field $B_\varphi = \pm B_z$ (plus is for $y < 0$ and minus for $y < 0$) in units of Tesla at $\tau = 45.0$. Figure 2(c) gives the theoretical distribution of B_φ as indicated in Eq. (8) with the same parameters as in the simulations. It can be seen that the analytical model well reproduces the radiation pattern observed in the simulation. The intense spherical low-frequency electromagnetic wave is emitted from the exact center of the laser focus. The whole wave profile presents a single cycle type. The polarization of the magnetic field is along the φ direction and that of the electric field is along the θ direction, while other components are almost equal to zero (not shown). According to the direction of the radiated field, we can infer the Poynting vector to be predominantly normal over a spherical wavefront. The intensity of radiation is not distributed uniformly over the spherical wavefront, but is obviously dependent on the emission angle. Figure 2(d) shows the energy angular distribution of B^2_φ (red solid line) at the vacuum semi-circle with radius $R = 35$, together with the fitting to sin-square function (blue dashed line). The angular distribution matches well with sin-square fitting, which is the typical distribution for a charged particle traveling non-relativistically in a straight line, as indicated by Eq. (8). The radiation peaks at the direction along the plasma-vacuum interface and decreases to zero at the target normal direction, naturally separated from the reflected laser pulse and harmonics.

We define the field quality $F_\pm = (E_\theta/c \pm B_\varphi)/2$, which describes the flux of radiation propagating in $\pm r$ directions. The inset plot in Fig. 2(e) shows the single-cycle time waveform of $F_\pm$ (red line) recorded in simulation at the observation point at $R = 30$ on the target surface. The fact that F (red dashed line) equals zero proves that radiation flows in the positive r direction. The whole F_+ time spectrum (red solid line) lasts about $30T$ from about $\tau = 30$ to $\tau = 60$, almost as the same as the duration of the laser pulse. The blue solid line gives the theoretical spectrum indicated by Eq. (8), in which A_x is numerically calculated by Eq. (10). The satisfactory consistence of the simulation spectrum with the model confirms the reliability of the theoretical model. The field peak is about 24.0 Tesla, corresponding to 72.0 MV/cm. The corresponding frequency spectrum of F_+ is shown in the main plot in Fig. 2(e). The spectrum covers a range from 0 up to ~ 30 THz, with its peak at ~ 12.0 THz, which roughly equals the carrier frequency of the laser pulse envelope. The frequency of THz radiation can be easily controlled by adjusting the laser duration.

For sharp-edged plasma, when laser is normally incident with intensity above 10^{18} W·cm^{-2}, the $\boldsymbol{j} \times \boldsymbol{B}$ mechanism would dominate the energy absorption. Other collisionless mechanisms, such as vacuum heating and resonance absorption, are not evident because no electric field is parallel to the density gradient. Figure 3(a) shows the longitudinal trajectory of electrons at the exact center of the laser focus. All electrons are flowing slowly along the theoretical trajectory (red solid line) predicted by Eq. (5). Even though these electrons experience evident double-frequency oscillation, it is worth noting that the electrons are confined in laser field and are not effec-

tively heated. Figures 3(b) and 3(c) show the momentum spectrum of electrons at two successive quarter periods $\tau = 14.75$ and $\tau = 15.00$, respectively. At $\tau = 14.75$, all electrons in the compression zone are pushed forward, while during the next $1/4T_0$, they are completely dragged back. Electrons seldom turn to be thermal by escaping from the laser field. Because of the orderly collective movement of surface electrons under the constraints of laser and electrostatic pressure, the waveform of THz radiation is quite clear, which cannot be achieved by the thermal electron bunch with large divergence and somewhat stochastic motion.

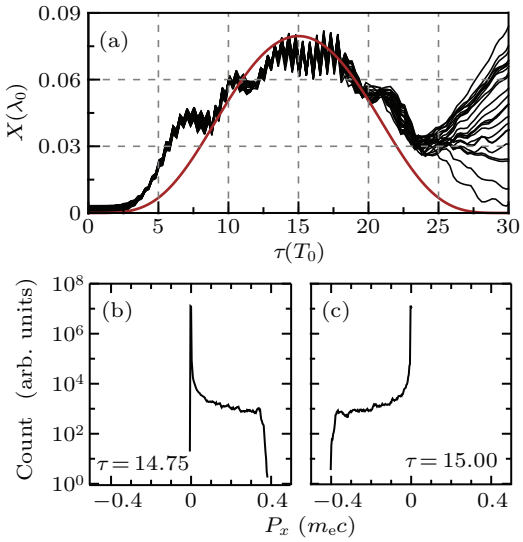


Fig. 3. (a) The longitudinal trajectory of the surface electron located at the exact center of laser focus for simulation (black lines) and theory (red line). (b) and (c) The momentum spectra of electrons at two successive quarter periods.

The influence of laser intensity and plasma density on THz radiation is further investigated by PIC simulations. Figure 4 gives the snapshot of B_φ at $\tau = 45.0$ for (a) $a_0 = 2.0$, $N_0 = 2.0$, (b) $a_0 = 1.0$, $N_0 = 4.0$, (c) $a_0 = 5.0$, $N_0 = 10.0$, and their corresponding electron trajectories in (d), (e), and (f). Different from Fig. 2(a), due to the emergency of thermal electrons for all these three cases here, disordered radiations on both the front and the back sides of the plasma slab are observed. For $a_0 = 2.0$, $N_0 = 2.0$ in Fig. 4(a), numerous thermal electrons are generated due to the relativistically self-induced transparency (RST) resulting from the relativistic increase of inertial electron mass by $\gamma = \sqrt{1 + a_0^2}$. The relativistic plasma frequency reduces to $\omega_p'^2 = \omega_p^2/\gamma = N_0\omega_0^2/\sqrt{1 + a_0^2}$, where $\omega_p = \sqrt{n_e e^2/m_e\varepsilon_0}$ is the non-relativistic plasma frequency. The threshold condition for RST is $\omega_p' = \omega_0$, i.e., $a_0^2 = N_0^2 - 1$. When laser intensity is enhanced or plasma density is reduced to meet the threshold value, the laser would penetrate through the plasma slab and lead to the generation of thermal electrons. For $a_0 = 1.0$, $N_0 = 4.0$ in Fig. 4(b), although the slab is opaque for the driving laser, the plasma wave would resonant dramatically with $2\omega_0$ oscillating component of $\boldsymbol{j} \times \boldsymbol{B}$ force, so electrons are more likely to free themselves from the laser field and penetrate deeply into plasma. For higher plasma density and laser intensity such as $a_0 = 5.0$, $N_0 = 10.0$ in Fig. 4(c), although the similarity parameter $S = n_0/a_0 n_c$ keeps unchanged with $a_0 = 1.0$ and $N_0 = 2.0$, the waveform of radiation is much more disordered. The trajectories of these electrons are similar to those in the work of Chen *et al.*[39] in solid density regime. For both the situations, the Rayleigh–Taylor-type instability and the strong heating of electrons severely distort the longitudinal single-cycle motions of surface electrons. The amplitude of the oscillation for a large number of fast electrons reaches several wavelengths. When these fast electrons pass through the target-vacuum interface, the transition radiations are emitted, as observed in Ref. [21]. The radiation noises from fast electrons reduce the radiation cleanliness.

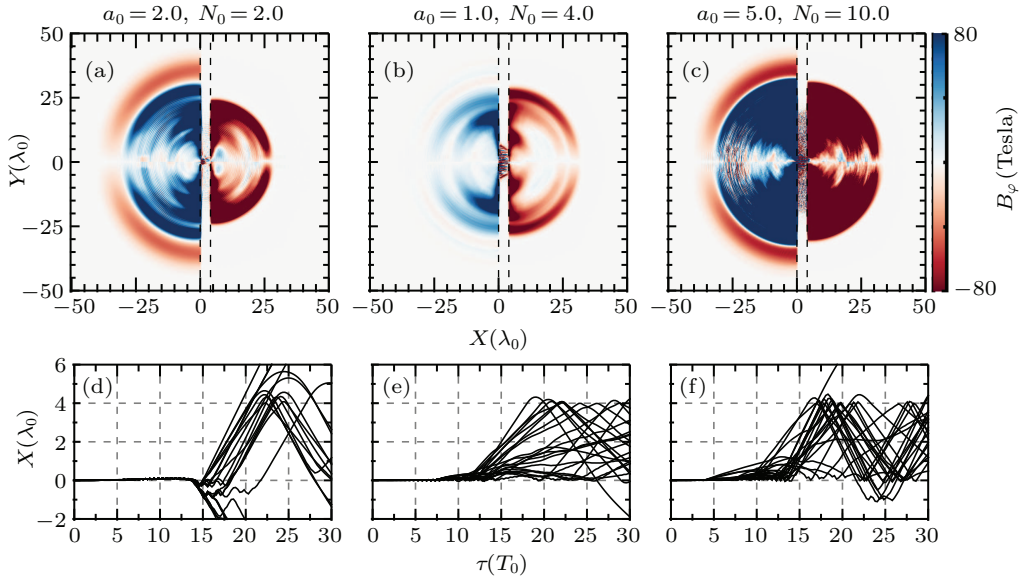


Fig. 4. The snapshots for B_φ [(a)–(c)] and the corresponding longitudinal trajectory of electrons [(d)–(f)] for $a_0 = 2.0$, $N_0 = 2.0$ (left column), $a_0 = 1.0$, $N_0 = 4.0$ (middle column) and $a_0 = 5.0$, $N_0 = 10.0$ (right column).

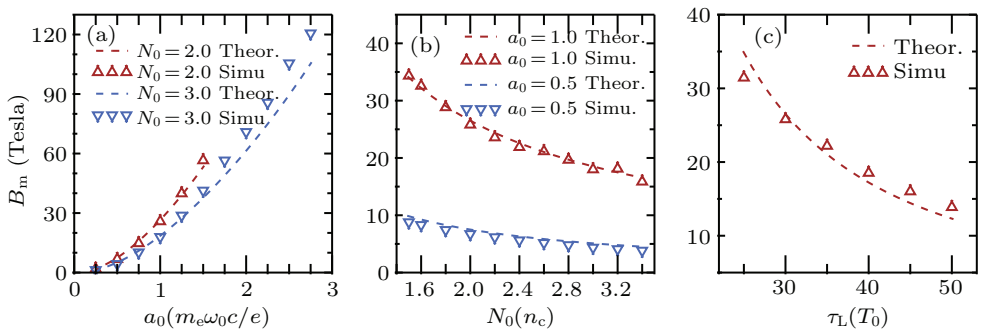


Fig. 5. Parametric dependence of the maximal magnetic field as a function of laser intensity (a), electron density (b), and pulse duration (c). The dashed lines represent model prediction, and the triangles represent simulation results. The parameters not mentioned in each plot are the same as those in Fig. 2.

Finally, we change the simulation parameters systematically and compare the results with Eq. (8). Figure 5(a) gives the dependence of maximal magnetic field B_m on laser intensity a_0 ($a_0 < \sqrt{N_0^2-1}$) for $N_0 = 2.0$ (red up triangle) and $N_0 = 3.0$ (blue down triangle). The radiation field strength monotonically increases with laser energy, which is well consistent with the theory (dashed line). Notice that for $N_0 = 3.0$ and $a_0 = 2.75$, the maximal magnetic field at $R = 30.0$ reaches up to 118.0 T (electric field is 354.0 MV/cm). The corresponding maximal radiation energy per solid angle is 0.15 mJ/sr. Figure 5(b) shows the relationship between B_m and electron density N_0 for $a_0 = 0.5$ (blue down triangle) and $a_0 = 1.0$ (red up triangle). B_m is almost inversely proportional to N_0, which is also in good agreement with the theoretical value. For the same laser intensity, lower density shows higher energy conversion efficiency. Figure 5(c) presents the dependence of B_m on laser duration τ_L. A shorter pulse duration is more beneficial for intense THz emission because the surface oscillation would be more drastic. Unfortunately, when the laser pulse is too short, there would be a deviation from our estimation, because the quasi-static balance is not satisfied under such extreme circumstance.

In theory, we assume that the ions are immobile. To suppress the movement of ions, the plasma targets with heavier ions are preferred. Simulations show that the movement of ions can be ignored in our laser parameter regime because the ion mass is over 50 u (u is the atomic mass unit), such as xenon. We also study the influence of preplasma on the properties of THz radiation. The targets with preplasma of linear density are used in the simulations. The results do not change significantly as long as the scale length of the preplasma is below 200 nm, which is easy to realize by the current plasma mirror technique. If the preplasma is too long, severe laser absorption would occur.

Finally, we discuss the experimental feasibility of our scheme. In the experiment, it is of challenge to obtain plasma with a fairly uniform density in the near-critical range, because the critical density is too high compared with the gas density and too low compared with the solid density. At present, most targets with near-critical density are porous,[40,41] which is unsuitable for this THz generation scheme which requires uniform density. A well-designed gas nozzle[32] can produce a uniform supersonic gas jet with a density slightly lower than the critical density, and it can be further compressed into a gas slab with a higher density by two counter-propagating blast waves launched by nanosecond laser beams propagating along the side of the jet.[42] This may be a proper approach to achieve the plasma slab with near-critical density and sharp edge in our scheme.

4. Conclusion

In summary, we have demonstrated a scheme to generate low-noise, powerful and tunable THz radiation by using relativistic laser impinging on a NCD plasma slab. The THz strength obtained is proportional to the driving laser intensity and inversely proportional to the plasma density. The numerical results indicate that the proper parameter region is as follows: the plasma density is between $1.0n_c - 4.0n_c$ and the laser intensity should satisfy $a_0^2 < N_0^2 - 1$. In this parameter regime, electrons will move in a collective form which eliminates the complex movement of thermal electrons, resulting in a fairly clear THz radiation waveform. This intense THz radiation with peak strength around 100 MV/cm makes it a useful optical tool in nonlinear THz physics.

Acknowledgements

Project supported by the National Natural Science Foundation of China (Grant Nos. 11774430, 12075157, 11775202, and 12175310), and the Scientific Research Foundation of Hunan Provincial Education Department (Grant No. 20A042).

References

[1] Tonouchi M 2007 *Nat. Photon.* **1** 97
[2] Dhillon S, Vitiello M, Linfield E, Davies A, Hoffmann M C, Booske J, Paoloni C, Gensch M, Weightman P and Williams G 2017 *J. Phys. D: Appl. Phys.* **50** 043001
[3] Mankowsky R, Först M and Cavalleri A 2016 *Rep. Prog. Phys.* **79** 064503
[4] Liu M, Hwang H Y, Tao H, Strikwerda A C, Fan K, Keiser G R, Sternbach A J, West K G, Kittiwatanakul S and Lu J 2012 *Nature* **487** 345

[5] Cavalleri A 2018 *Contemp. Phys.* **59** 31

[6] Qi T T, Shin Y H, Yeh K L, Nelson K A and Rappe A M 2009 *Phys. Rev. Lett.* **102** 247603

[7] Hafez H, Chai X, Ibrahim A, Mondal S, Férachou D, Ropagnol X and Ozaki T 2016 *J. Opt.* **18** 093004

[8] Zhang Y, Li K and Zhao H 2020 *Front. Optoelectron.* **14** 4

[9] Wang D, Wang X, Liao G, Zhang Z and Li Y 2022 *Chin. Phys. B* **31** 056103

[10] Nanni E A, Huang W R, Hong K H, Ravi K, Fallahi A, Moriena G, Miller R D and Kärtner F X 2015 *Nat. Commun.* **6** 8486

[11] Walsh D, Lake D, Snedden E, Cliffe M, Graham D and Jamison S 2017 *Nat. Commun.* **8** 421

[12] Curry E, Fabbri S, Maxson J, Musumeci P and Gover A 2018 *Phys. Rev. Lett.* **120** 094801

[13] Hibberd M T, Healy A L, Lake D S, Georgiadis V, Smith E J H, Finlay O J, Pacey T H, Jones J K, Saveliev Y, Walsh D A, Snedden E W, Appleby R B, Burt G, Graham D M and Jamison S P 2020 *Nat. Photon.* **14** 755

[14] Zhang G B, Hafz N A M, Ma Y Y, Qian L J, Shao F Q and Sheng Z M 2016 *Chin. Phys. Lett.* **33** 095202

[15] Hoffmann M C, Schulz S, Wesch S, Wunderlich S, Cavalleri A and Schmidt B 2011 *Opt. Lett.* **36** 4473

[16] Wu Z, Fisher A S, Goodfellow J, Fuchs M, Daranciang D, Hogan M, Loos H and Lindenberg A 2013 *Rev. Sci. Instrum.* **84** 022701

[17] Vicario C, Jazbinsek M, Ovchinnikov A, Chefonov O, Ashitkov S, Agranat M and Hauri C 2015 *Opt. Express* **23** 4573

[18] Shalaby M and Hauri C P 2015 *Nat. Commun.* **6** 5976

[19] Fülöp J A, Tzortzakis S and Kampfrath T 2020 *Adv. Opt. Mater.* **8** 1900681

[20] Liao G and Li Y 2019 *IEEE Trans. Plasma Sci.* **47** 3002

[21] Ding W J, Sheng Z M and Koh W S 2013 *Appl. Phys. Lett.* **103** 204107

[22] Liao G Q, Li Y T, Zhang Y H, Liu H, Ge X L, Yang S, Wei W Q, Yuan X H, Deng Y Q, Zhu B J, Zhang Z, Wang W M, Sheng Z M, Chen L M, Lu X, Ma J L, Wang X and Zhang J 2016 *Phys. Rev. Lett.* **116** 205003

[23] Liao G, Li Y, Liu H, Scott Graeme G, Neely D, Zhang Y, Zhu B, Zhang Z, Armstrong C, Zemaityte E, Bradford P, Huggard Peter G, Rusby Dean R, McKenna P, Brenner Ceri M, Woolsey Nigel C, Wang W, Sheng Z and Zhang J 2019 *Proc. Natl. Acad. Sci. USA* **116** 3994

[24] Zhang S, Yu J, Shou Y, Gong Z, Li D, Geng Y, Wang W, Yan X and Lin C 2020 *Phys. Plasma* **27** 023101

[25] Jin Z, Zhuo H B, Nakazawa T, Shin J H, Wakamatsu S, Yugami N, Hosokai T, Zou D B, Yu M Y, Sheng Z M and Kodama R 2016 *Phys. Rev. E* **94** 033206

[26] Gopal A, Herzer S, Schmidt A, Singh P, Reinhard A, Ziegler W, BrÖmmel D, Karmakar A, Gibbon P and Dillner U 2013 *Phys. Rev. Lett.* **111** 074802

[27] Gopal A, May T, Herzer S, Reinhard A, Minardi S, Schubert M, Dillner U, Pradarutti B, Polz J and Gaumnitz T 2012 *New J. Phys.* **14** 083012

[28] Herzer S, Woldegeorgis A, Polz J, Reinhard A, Almassarani M, Beleites B, Ronneberger F, Grosse R, Paulus G and Hübner U 2018 *New J. Phys.* **20** 063019

[29] Gopal A, Woldegeorgis A, Herzer S and Almassarani M 2019 *Phys. Rev. E* **100** 053203

[30] Woldegeorgis A, Herzer S, Almassarani M, Marathapalli S and Gopal A 2019 *Phys. Rev. E* **100** 053204

[31] Liao G Q, Liu H, Scott G G, Zhang Y H, Zhu B J, Zhang Z, Li Y T, Armstrong C, Zemaityte E, Bradford P, Rusby D R, Neely D, Huggard P G, McKenna P, Brenner C M, Woolsey N C, Wang W M, Sheng Z M and Zhang J 2020 *Phys. Rev. X* **10** 031062

[32] Henares J, Puyuelo Valdes P, Hannachi F, Ceccotti T, Ehret M, Gobet F, Lancia L, Marquès J R, Santos J and Versteegen M 2019 *Rev. Sci. Instrum.* **90** 063302

[33] Jun L Y, Ning Y D, Qing D Y, Xu Z, Qing W W, Lei G X, Hui Y X, Feng L and Ming C L 2019 *Acta Phys. Sin.* **68** 155201 (in Chinese)

[34] Yu W, Yu M Y, Sheng Z M and Zhang J 1998 *Phys. Rev. E* **58** 2456

[35] Macchi A, Cattani F, Liseykina T V and Cornolti F 2005 *Phys. Rev. Lett.* **94** 165003

[36] Ji L, Shen B, Zhang X, Wen M, Xia C, Wang W, Xu J, Yu Y, Yu M and Xu Z 2011 *Phys. Plasma* **18** 083104

[37] Jackson J D 1998 *Classical Electrodynamics* 3rd edn. (New York: John Wiley & Sons) p. 663

[38] Arber T D, Bennett K, Brady C S, Lawrence-Douglas A, Ramsay M G, Sircombe N J, Gillies P, Evans R G, Schmitz H, Bell A R and Ridgers C P 2015 *Plasma Phys. Control. Fusion* **57** 113001

[39] Chen Z Y, Li X Y and Yu W 2013 *Phys. Plasma* **20** 103115

[40] Jiang B, He C, Zhao N, Nash P, Shi C and Wang Z 2015 *Sci. Rep.* **5** 13825

[41] Maffini A, Pazzaglia A, Dellasega D, Russo V and Passoni M 2019 *Phys. Rev. Mater.* **3** 083404

[42] Marquès J R, Loiseau P, Bonvalet J, Tarisien M, d'Humières E, Domange J, Hannachi F, Lancia L, Larroche O and Nicola P 2021 *Phys. Plasma* **28** 023103